PAPER

Check for updates

Highly selective electrocatalytic reduction of CO₂ to HCOOH over an *in situ* derived Ag-loaded Bi₂O₂CO₃ electrocatalyst†

Wei Zheng, [iD] ‡[a] Changlai Wang,‡[a] Jing Chen,[a] Shi Chen, [iD] [a] Zhiyu Lin, [iD] [a] Minxue Huang, [iD] [a] Hao Huang, [iD] [a] Yafei Qu,[a] Peichen Wang, [iD] [a] Lin Hu★[b] and Qianwang Chen [iD] ★[a,b]

The electrochemical reduction of CO₂ to HCOOH is considered one of the most appealing routes to alleviate the energy crisis and close the anthropogenic CO₂ cycle. However, it remains challenging to develop electrocatalysts with high activity and selectivity towards HCOOH in a wide potential window. In this regard, Ag/Bi₂O₂CO₃ was prepared by an *in situ* electrochemical transformation from Ag/Bi₂O₃. The Ag/Bi₂O₂CO₃ catalyst achieves a faradaic efficiency (FE) of over 90% for HCOOH in a wide potential window between −0.8 V and −1.3 V *versus* the reversible hydrogen electrode (RHE). Moreover, a maximum FE of 95.8% and a current density of 15.3 mA cm⁻² were achieved at a low applied potential of −1.1 V. Density functional theory (DFT) calculations prove that the high catalytic activity of Ag/Bi₂O₂CO₃ is ascribed to the fact that Ag can regulate the electronic structure of Bi, thus facilitating the adsorption of *OCHO and hindering the adsorption of *COOH. This work expands the *in situ* electrochemical derivatization strategy for the preparation of electrocatalysts.

Introduction

The environmental problems caused by CO₂ emission are threatening the sustainable development of human society.[1] The CO₂ reduction reaction (CO₂RR) powered by renewable electricity is considered a potential strategy to offset these issues.[2,3] Generally, diverse conversion products, such as CO, HCOOH, CH₄, C₂H₄ and C₂H₅OH, can be obtained from the CO₂RR.[4–8] Among these products, liquid HCOOH is more favoured due to its high commercial value and convenience for transportation and storage.[9]

The selectivity of the CO₂RR catalyst is believed to be determined by the adsorption energy of *COOH, *OCHO and *H intermediates. Some main group metal elements including Pb, Sn, In, and Sb, which thermodynamically favour the adsorption of *OCHO over *COOH, are efficient electrocatalysts for converting CO₂ into HCOOH (Table S1†). However, high toxicity and high cost are two barriers to their large-scale appli-

cations. In contrast, as a low-cost and environmentally benign electrocatalyst, Bi has also received much attention for the conversion of CO₂ to HCOOH.[10–12] Unfortunately, the harsh reaction conditions become a hindrance to its further development. Specifically, Bi-based electrocatalysts are limited by a narrow potential window for high selectivity and poor stability (Table S2†). For example, Bi nanosheets and Bi nanoparticles can only achieve high selectivity (FE > 90%) in a potential window of nearly 300 mV.[13,14] On the one hand, the poor stability of *OCHO hinders the formation of HCOOH at low overpotentials. Moreover, H₂ and CO ineluctably occupy a larger proportion with increasing cathodic potentials. To this end, its *OCHO adsorption energy remains to be optimized to achieve better selectivity towards HCOOH in a wider working potential. Recent research on Bi-based catalysts demonstrated that bismuth oxide catalysts exhibit better selectivity than metallic Bi because the Bi–O structure is more favourable to stabilize the *OCHO intermediate.[15] Among all the Bi-based materials, the valence state of Bi ions in Bi₂O₂CO₃ is higher than that of Bi₂O₃. While the electron transfer between Bi₂O₂CO₃ and heteroatoms could further modulate the electronic structure of Bi to an optimal level for the adsorption of *OCHO. For example, Ag metal has poor adsorption toward hydrogen, which makes it a good choice to be used in the CO₂RR to stabilize *OCHO and suppress the by-reaction HER.[16]

Therefore, Ag loaded Bi₂O₂CO₃ could be a high activity catalyst for the conversion of CO₂ to HCOOH. Here, we prepared

[a]*Hefei National Research Center for Physical Sciences at the Microscale and Department of Materials Science & Engineering, University of Science and Technology of China, Hefei 230026, China. E-mail: cqw@ustc.edu.cn*
[b]*The High Magnetic Field Laboratory, Chinese Academy of Sciences, Hefei 230031, China*
†Electronic supplementary information (ESI) available. See DOI: https://doi.org/10.1039/d3dt04342h
‡These authors contributed equally to this work.

Ag/Bi_2O_3 nanosheets, which could undergo a carbonatization process in $KHCO_3$ electrolyte to generate $Ag/Bi_2O_2CO_3$. The *in situ* formed catalysts are believed to possess a lower contact resistance and more active sites. $Ag/Bi_2O_2CO_3$ demonstrates high selectivity toward HCOOH over a wide potential window. Theoretical calculations suggest that the CO and H_2 pathways are repressed due to the optimized adsorption of *OCHO on $Ag/Bi_2O_2CO_3$. The *in situ* attenuated total reflection Fourier transform infrared (ATR-FTIR) analysis shows that *CO has a much weaker signal than *OCHO. In addition, durability tests prove that it can maintain an approximate 90% FE towards HCOOH (FE_{HCOOH}) at a current density of -13.0 mA cm^{-2} in 10 h.

Experimental section

Characterization

The powder X-ray diffraction (XRD) patterns of the samples were collected on a Japan Rigaku D/MAX-γA X-ray diffractometer equipped with Cu Kα radiation ($\lambda = 1.54178$ Å) at a scanning rate of 5° min^{-1} in the 2θ range from 20 to 80°. Scanning electron microscopy (SEM) images were recorded on a Zeiss Supra 40 field-emission scanning microscope operating at 5 kV. Transmission electron microscopy (TEM) images were collected on a Hitachi H-7650 transmission electron microscope using an accelerating voltage of 100 kV and high-resolution transmission electron microscopy (HRTEM) images were recorded on a FEI Talos F200X at an accelerating voltage of 200 kV. Inductively coupled plasma-atomic emission spectrometry (ICP-AES) was conducted with an Optima 7300 DV instrument. XPS was performed on an ESCALAB 250 X-ray photoelectron spectrometer using Al Kα radiation. The C 1s peak at 284.8 eV is used as a reference to correct the binding energy shift caused by the charge effect. The X-ray absorption near edge structures (XANES) of Ag K-edge and Bi L-edge were measured at the BL14W1 beamline of the Shanghai Synchrotron Radiation Facility (SSRF).

Electrochemical measurements

The electrochemical measurements were conducted at 25 °C using an electrochemical workstation (CHI760E) in a three-electrode, two-compartment H-type electrolysis cell. Each compartment of the H-type cell contained 30 mL of 0.5 M $KHCO_3$ solution. Pt foil and a Ag/AgCl (saturated KCl) electrode were employed as the counter and reference electrodes, respectively. Before the investigation of the electrochemical CO_2RR, a flow of high-purity CO_2 at a flow rate of 30 sccm (standard cubic centimeter per minute) was purged into the 0.5 M $KHCO_3$ solution for 30 min to remove all the oxygen from the electrolyte and achieve CO_2 saturation. Cyclic voltammetry (CV) and linear sweep voltammetry (LSV) measurements were carried out in the 0.5 M $KHCO_3$ solution saturated with Ar/CO_2. CV was conducted for ten cycles at a scan rate of 100 mV s^{-1} in the potential range from -1.5 V to -0.3 V. Linear sweep voltammetry (LSV) was performed at a scan rate of 50 mV s^{-1}. Multiple potential step I–t measurements with several selected potentials were performed. All potentials were measured against an Ag/AgCl reference electrode and converted to the RHE scale based on the Nernst equation ($E_{RHE} = E_{Ag/AgCl} + 0.059 \times pH + 0.197$). The pH value of the Ar/CO_2-saturated 0.5 M $KHCO_3$ electrolyte solution is about 8.8/7.2.

Product analysis

The gas produced during the reaction was carried by high-pure CO_2 and analyzed by gas chromatography (Agilent 7890B) equipped with both a thermal conductivity detector (TCD) and a flame ionization detector (FID). The TCD was used to quantify H_2 and the FID was used to quantify CO and hydrocarbons. The faradaic efficiency (FE) of the gas product was calculated on the basis of the following equation:

$$FE = i_x/i_{tot} = z_x \times v_{gas} \times c_x \times F/(i_{tot} \times V_m)$$

where i_x is the partial current of product x, i_{tot} is the total current, z_x represents the number of electrons transferred towards the formation of 1 mol of product x, v_{gas} is the CO_2 flow rate (30 sccm), c_x represents the concentration of product x detected by gas chromatography (ppm), F is the Faraday constant (96 485 C mol^{-1}), and V_m is the unit molar volume, which is 24.5 L mol^{-1} at room temperature (298.15 K). The liquid in the working compartment of the H-cell was collected and analyzed by ^{1}H nuclear magnetic resonance (^{1}H-NMR). ^{1}H-NMR samples were prepared by mixing 1 mL of the collected solution with 50 μL D_2O and 10 μL of 2000 ppm DMSO as an internal standard. The FE for formate is calculated as follows:

$$\begin{aligned} FE &= i_{formate}/i_{tot} \\ &= z \times n_{DMSO} \times 6 \times F \times S_{DMSO}/(i_{tot} \times S_{formate} \times t) \end{aligned}$$

where $i_{formate}$ is the partial current of formate, i_{tot} is the total current, z represents the number of electrons transferred towards the formation of formate ($z = 2$), n_{DMSO} is the mole of DMSO, F is the Faraday constant (96 485 C mol^{-1}), S_{DMSO} and $S_{formate}$ are the peak areas of DMSO and formate in ^{1}H-NMR spectra, respectively, and t is the time of each test.

In situ ATR-FTIR test

In situ ATR-FTIR spectroscopy was carried out using a Thermo Fisher NICOLET iS50 FTIR and the measured potential for the CO_2RR was in the potential range between 0 V and -1.2 V controlled by an electrochemical workstation (CHI760E). The *in situ* electrochemical three-electrode cell contained $Ag/Bi_2O_2CO_3$ as the working electrode, Ag/AgCl as the reference electrode and Pt wire as the counter electrode. The electrolyte used was CO_2-saturated 0.5 M $KHCO_3$.
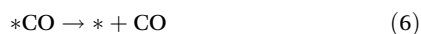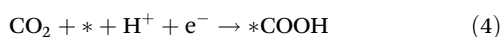
DFT calculations

All calculations were carried out based on density functional theory (DFT) as implemented in the Vienna *Ab initio* Simulation Package (VASP).[17] The projector augmented wave (PAW) pseudopotentials were used to treat the core electrons, while the Perdew–Burke–Ernzerhof (PBE) functional within the

generalized gradient approximation (GGA) was used for describing the electron interactions.[18,19] The cutoff energy was set to 400 eV. The convergence of total energy and forces was set to 1×10^{-5} eV and 0.01 eV Å^{-1}, respectively. A grid of $3 \times 3 \times 1$ Monkhorst–Pack k-points was used for the structural relaxation. A vacuum layer of 15 Å was adopted in the direction perpendicular to the surface to avoid interactions between periodic slabs. The reaction pathway of CO_2-to-HCOOH involves the following elementary step, where the symbol '*' represents the active site.

$$CO_2 + * + H^+ + e^- \rightarrow *OCHO \tag{1}$$

$$*OCHOH + H^+ + e^- \rightarrow *HCOOH \tag{2}$$

$$*HCOOH \rightarrow * + HCOOH \tag{3}$$
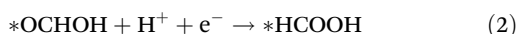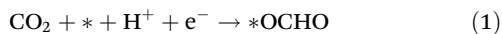
And the reaction pathway of CO_2-to-CO is as follows:

$$CO_2 + * + H^+ + e^- \rightarrow *COOH \tag{4}$$

$$*COOH + H^+ + e^- \rightarrow *CO + H_2O \tag{5}$$

$$*CO \rightarrow * + CO \tag{6}$$

The Gibbs free energies were calculated as follows:

$$\Delta G = \Delta E + (\Delta ZPE - T\Delta S)$$

where ΔE is the adsorption or reaction energy based on DFT calculations, ΔZPE is the change in zero-point energy, T is the temperature (298.15 K), and ΔS is the change in entropy. The entropies of gas phases CO_2, H_2, CO, HCOOH and H_2O are obtained from the National Institute of Standards and Technology database under standard conditions.

Results and discussion

The synthetic route is depicted in Fig. 1a. Bi_2O_3 nanosheets were synthesized using a hydrothermal method at 160 °C for 1 h. Ag/Bi_2O_3 was prepared by a deposition–precipitation method. In short, Bi_2O_3 aqueous suspension was mixed with AgNO$_3$ solution so that Ag$^+$ could be loaded on the surface of Bi_2O_3. Then NaOH solution was added to the mixture, followed by centrifugation and heat treatment at 450 °C. The pre-catalyst Ag/Bi_2O_3 was transformed into Ag/$Bi_2O_2CO_3$ during the CO_2RR.

The as-synthesized Ag/Bi_2O_3 consists of assembled Bi_2O_3 nanosheets and Ag nanoparticles (Fig. 1b and S1†). The SEM and TEM images (Fig. 1b and S2†) revealed that the as-prepared Bi_2O_3, Ag/Bi_2O_3, and Ag/$Bi_2O_2CO_3$ exhibited nanosheet morphology. The Brunauer–Emmett–Teller (BET) specific surface areas of the Bi_2O_3 and Ag/Bi_2O_3 precursors were found to be 20.77 m^2 g^{-1} and 27.96 m^2 g^{-1}, respectively (Fig. S3 and S4†). The XRD patterns of the catalyst (Fig. S5 and S6†) matched with those of Ag and $Bi_2O_2CO_3$. Interplanar spacings of $Bi_2O_2CO_3$ (004) and Ag (111) were observed in the HRTEM images (Fig. 1c), indicating that Ag/$Bi_2O_2CO_3$ was generated after the CO_2RR. In Fig. 1d, the HAADF-STEM image proves that Ag/$Bi_2O_2CO_3$ is also an aggregate of nanosheets.

The elemental composition and chemical states of Ag/$Bi_2O_2CO_3$ were investigated by X-ray photoelectron spectroscopy (XPS). XPS results revealed that the sample contains Ag, Bi, C and O elements. The binding energy of Bi in Ag/$Bi_2O_2CO_3$ shows a positive shift compared to $Bi_2O_2CO_3$, thus Bi is in a higher valence state.[11] Moreover, Ag in Ag/$Bi_2O_2CO_3$ shifted to a lower binding energy compared to Ag nanoparticles (Ag NP), which indicates that Ag is also in a higher valence state.[20] The two peaks in the C 1s spectra (Fig. S7a†) were assigned to the carbon species absorbed on the surface of nanoparticles (284.6 eV) and $CO_3{}^{2-}$ (288.6 eV), respectively. In Fig. S7b,† three peaks of O 1s were matched to Bi–O bonds (529.2 eV), $CO_3{}^{2-}$ (530.4 eV), and absorbed water (532.2 eV).[21] The O 1s spectra show that the Bi–O peak and the $CO_3{}^{2-}$ peak of Ag/$Bi_2O_2CO_3$ shifted to a lower binding energy compared to $Bi_2O_2CO_3$. Therefore, XPS results confirmed that the electrons were transferred from Ag and Bi to O. The electronic state and atomic environment of Bi were further verified by performing X-ray adsorption near-edge structure (XANES) measurements. As shown in Fig. 2c and Fig. S8,† the XANES spectra show that the adsorption edge of Ag/$Bi_2O_2CO_3$ shifted to a higher energy compared to that of Bi_2O_3, indicating that the valence of Bi in Ag/$Bi_2O_2CO_3$ is higher than that of Bi_2O_3.[22] In Fig. 2d, the adsorption edge of Ag/$Bi_2O_2CO_3$ shows a blue shift compared to Ag foil, which is in agreement with the results of XPS analysis presented in Fig. 2a and b. Furthermore, we analysed k^2-weighted Bi L$_3$-edge EXAFS wavelet transform plots of Bi_2O_3 and Ag/$Bi_2O_2CO_3$ (Fig. 2e) to determine their coordination environment.[23,24] The scattering path signal of Bi–O–C was observed. For k^2-weighted Ag K-edge EXAFS wavelet transform plots of Ag foil and Ag/$Bi_2O_2CO_3$ (Fig. S9†), the existence of the Ag–Ag and Ag–O structures was confirmed, proving that Ag is loaded on the surface of $Bi_2O_2CO_3$ instead of being doped into the $Bi_2O_2CO_3$ lattice.

The electrochemical activities of $Bi_2O_2CO_3$ and Ag/$Bi_2O_2CO_3$ were first evaluated by linear sweep voltammetry (LSV) in Ar and CO_2 purged 0.5 M KHCO$_3$ (Fig. 3a). Ag/$Bi_2O_2CO_3$ demonstrates a larger current density than $Bi_2O_2CO_3$ in CO_2 purged 0.5 M KHCO$_3$. Compared to Ag/$Bi_2O_2CO_3$, $Bi_2O_2CO_3$ displays a slightly higher current density in Ar purged 0.5 M KHCO$_3$, which means the hydrogen evolution reaction (HER) on Ag/$Bi_2O_2CO_3$ is hindered. Moreover, constant potential electrolysis at different potentials has been adopted to evaluate their CO_2RR performance. $Bi_2O_2CO_3$ shows nearly 80% FE$_{HCOOH}$ at −1.0 V (Fig. S10†). Further introduction of Ag significantly increases the FE$_{HCOOH}$. In particular, the FE$_{HCOOH}$ of Ag/$Bi_2O_2CO_3$ was 95.8% at a potential of −1.1 V with a j_{HCOOH} of −15.3 mA cm^{-2} (Fig. 3b and c). Moreover, we also investigated the effect of Ag content on CO_2RR performance by testing samples with different Ag loadings (denoted as s-1, s-2 and s-3) (Table S3†). Among which, s-2 (0.384 wt% Ag) shows the best performance in terms of FE$_{HCOOH}$ (Fig. 3c and S10†). A high FE$_{HCOOH}$ (>90%) was also obtained for s-2 from −0.8 V to −1.3 V. In addition, there was no apparent change in selectivity and current density during the durability test, showing the outstanding stability of Ag/$Bi_2O_2CO_3$.
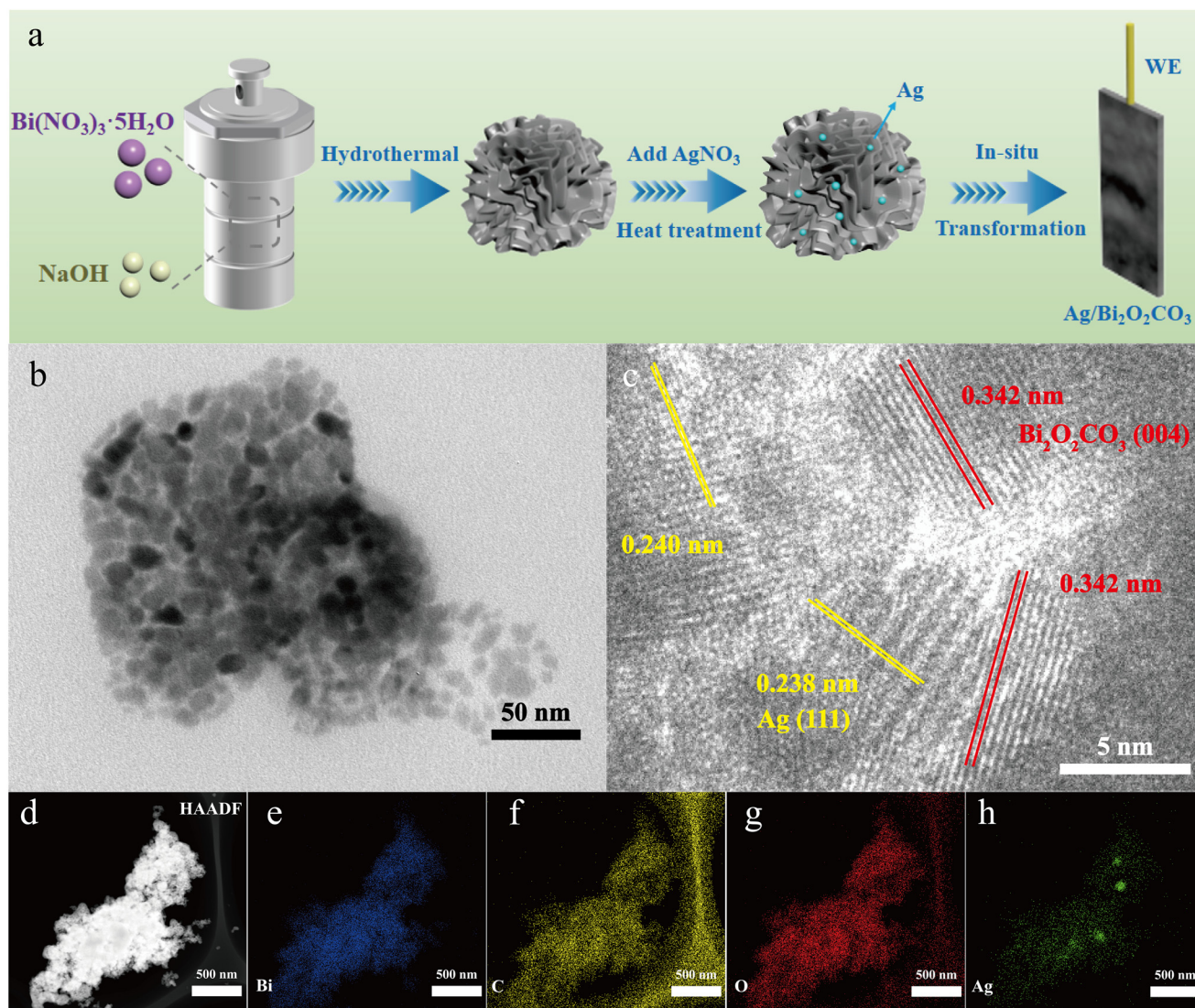
Fig. 1 (a) Scheme of Ag/Bi$_2$O$_2$CO$_3$ preparation. (b) TEM image of Ag/Bi$_2$O$_3$. (c) HRTEM image of Ag/Bi$_2$O$_2$CO$_3$. (d–h) HAADF-STEM images and elemental mapping of Ag/Bi$_2$O$_2$CO$_3$.

We carried out *in situ* ATR-FTIR analysis to identify the key intermediates of the CO$_2$RR (Fig. 3e and S11†). The peaks at 1620 and 1220 cm^{-1} are assigned to the bending vibration of H$_2$O and Si–O vibration from the silicon prism.[25] The peaks at 1430, 1725 and 2940 cm^{-1} become stronger as the applied potential decreases. These peaks can be assigned to the C–O, C=O and C–H vibrations of the *OCHO intermediate, respectively. The signal of *CO appears at 1880 cm^{-1} at high overpotentials, which means HCOOH is the main product during the CO$_2$RR.

The electrochemically active surface area (ECSA) was assessed by calculating the double-layer capacitance (C_{dl}). The value of C_{dl} was determined by cyclic voltammetry (CV) which was measured at different scan rates (Fig. S12†). As shown in Fig. 4a, Ag/Bi$_2$O$_2$CO$_3$ shows a higher C_{dl} value (6.45 mF cm^{-2}) than Bi$_2$O$_2$CO$_3$ (5.48 mF cm^{-2}). Such results indicate that Ag/ Bi$_2$O$_2$CO$_3$ has more exposed active sites than Bi$_2$O$_2$CO$_3$. The charge transfer resistances (R_{ct}) for Bi$_2$O$_2$CO$_3$ and Ag/Bi$_2$O$_2$CO$_3$ were determined by electrochemical impedance spectroscopy (EIS) measurements at −0.6 V (Fig. 4b). The R_{ct} value of Ag/ Bi$_2$O$_2$CO$_3$ is smaller than Bi$_2$O$_2$CO$_3$, indicating a faster interface charge transfer. Therefore, it would be easier for CO$_2$ to receive electrons from Ag/Bi$_2$O$_2$CO$_3$ to form the *OCHO intermediate.[26] As shown in Fig. 4c, Ag/Bi$_2$O$_2$CO$_3$ exhibited a lower Tafel slope (120.8 mV dec^{-1}) than Bi$_2$O$_2$CO$_3$ (175.8 mV dec^{-1}), revealing that more favourable CO$_2$RR kinetics was attained through the introduction of Ag. Noticeably, this value of 120.8 mV dec^{-1} for Ag/Bi$_2$O$_2$CO$_3$ was nearing 118 mV dec^{-1}, which means that the first formation of *OCHO was the rate-determining step (RDS).[27] Besides, the calculated j_{HCOOH} at −1.0 V delivered a first-order dependence on KHCO$_3$ concentration (Fig. 4d). These results further illustrated that H$^+$ that participated in the formation of the *OCHO intermediate originates from KHCO$_3$ rather than H$_2$O.[28]
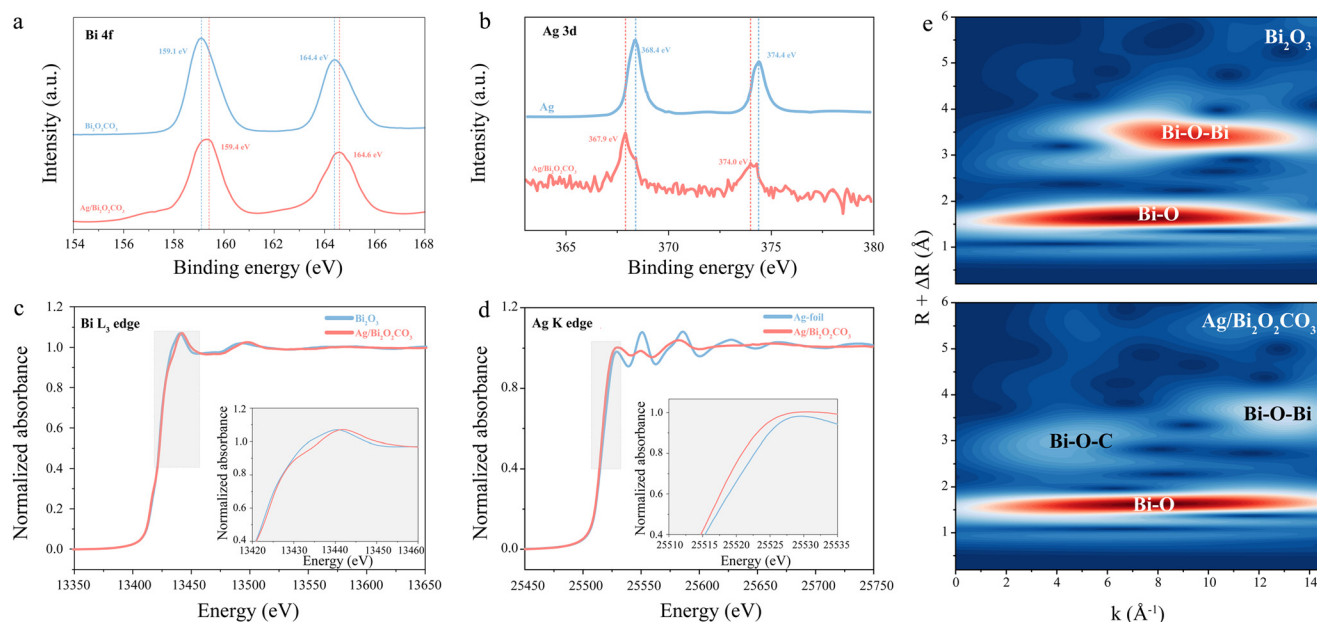
Fig. 2 (a) Bi 4f XPS spectra of $Bi_2O_2CO_3$ and $Ag/Bi_2O_2CO_3$. (b) Ag 3d XPS spectra of Ag foil and $Ag/Bi_2O_2CO_3$. (c) Bi L_3-edge XANES curves of Bi_2O_3 and $Ag/Bi_2O_2CO_3$. (d) Ag K-edge XANES curves of Ag foil and $Ag/Bi_2O_2CO_3$. (e) Bi L_3-edge EXAFS wavelet transform plots of Bi_2O_3 and $Ag/Bi_2O_2CO_3$.
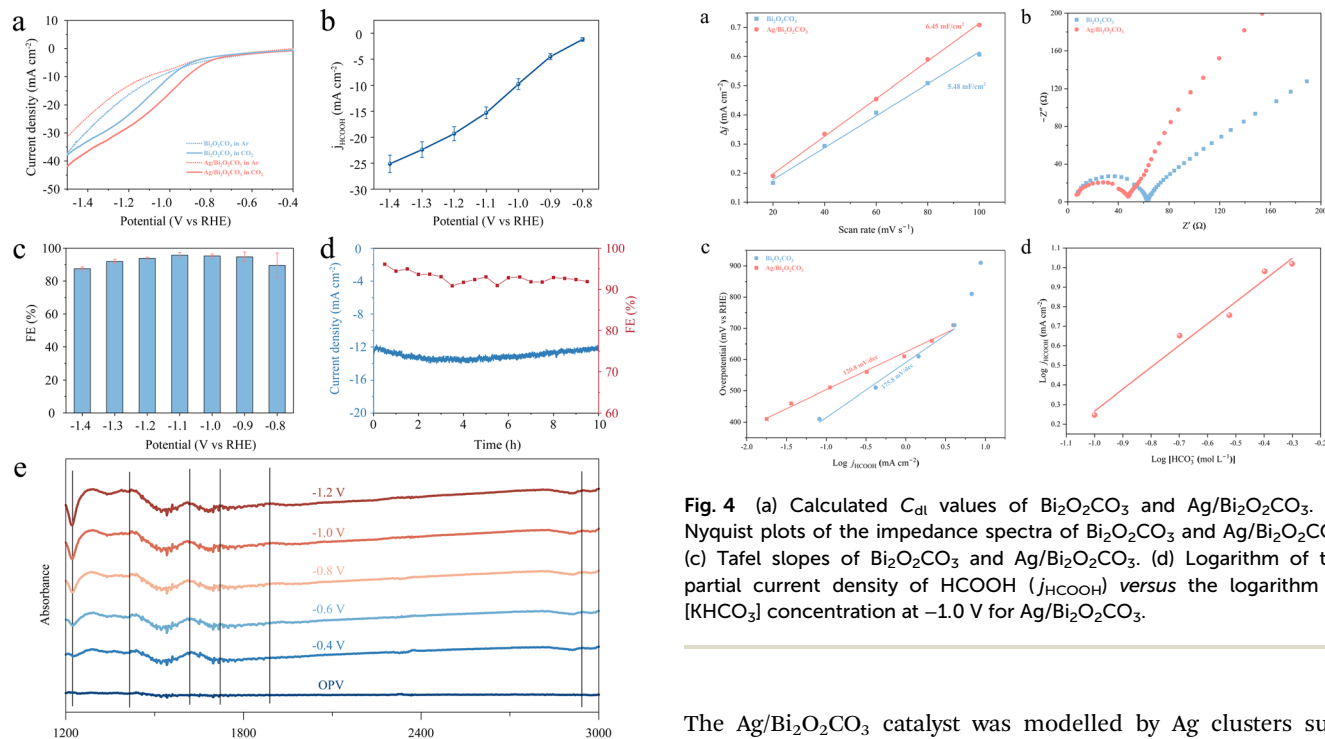
Fig. 3 (a) LSV of $Bi_2O_2CO_3$ and $Ag/Bi_2O_2CO_3$. (b) Partial current densities for HCOOH (j_{HCOOH}) of $Bi_2O_2CO_3$ and $Ag/Bi_2O_2CO_3$. (c) FE_{HCOOH} of $Ag/Bi_2O_2CO_3$ (s-2). (d) Durability test of $Ag/Bi_2O_2CO_3$ at −1.0 V for 10 h. (e) *In situ* ATR-FTIR spectra of $Ag/Bi_2O_2CO_3$.

Fig. 4 (a) Calculated C_{dl} values of $Bi_2O_2CO_3$ and $Ag/Bi_2O_2CO_3$. (b) Nyquist plots of the impedance spectra of $Bi_2O_2CO_3$ and $Ag/Bi_2O_2CO_3$. (c) Tafel slopes of $Bi_2O_2CO_3$ and $Ag/Bi_2O_2CO_3$. (d) Logarithm of the partial current density of HCOOH (j_{HCOOH}) *versus* the logarithm of [$KHCO_3$] concentration at −1.0 V for $Ag/Bi_2O_2CO_3$.

To further explore the reaction mechanism of the CO_2RR on the $Ag/Bi_2O_2CO_3$ catalyst, a theoretical investigation based on density functional theory (DFT) calculations was conducted. The $Ag/Bi_2O_2CO_3$ cataly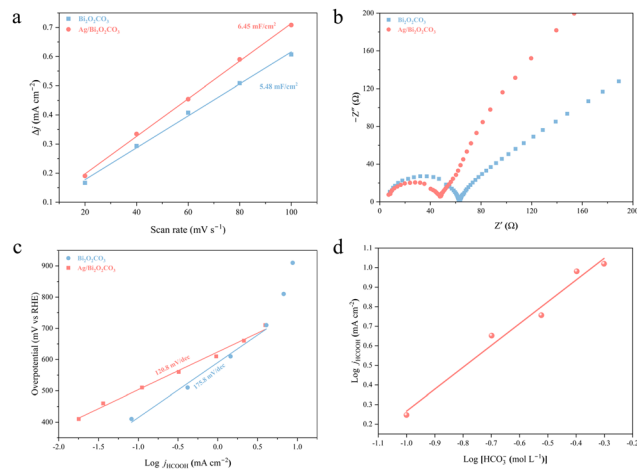st was modelled by Ag clusters supported on the $Bi_2O_2CO_3$ (100) surface (Fig. S13†). The reaction pathways of the CO_2RR to HCOOH and CO as well as the HER on $Ag/Bi_2O_2CO_3$ and $Bi_2O_2CO_3$ were considered. The Bi atoms adjacent to Ag clusters are the most active sites for HCOOH production. As shown in Fig. 5a and d, the RDS of the CO_2RR to HCOOH on $Ag/Bi_2O_2CO_3$ is the formation of *OCHO, requiring an energy barrier of 0.45 eV. And the formation of *COOH is the RDS of the CO_2RR to CO on $Ag/Bi_2O_2CO_3$, which needs to overcome an energy barrier of 2.12 eV (Fig. 5b and d).
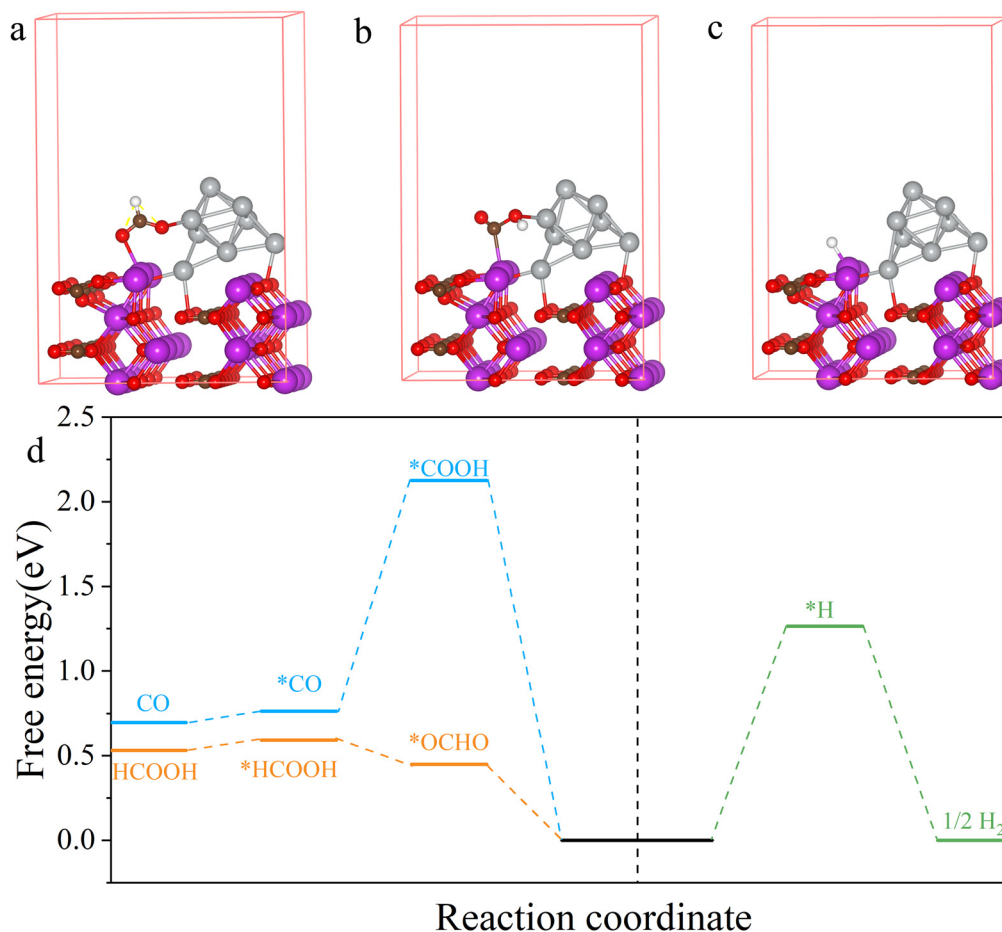
Fig. 5 The geometrical configuration of (a) *OCHO, (b) *COOH, (c) and *H over Ag/Bi$_2$O$_2$CO$_3$. The white, brown, red, grey, and purple spheres represent hydrogen, carbon, oxygen, silver, and bismuth atoms, respectively. (d) Free energy diagram of formate, carbon dioxide, and hydrogen formation over the Ag/Bi$_2$O$_2$CO$_3$ (100) surface.

Moreover, the energy barrier of the formation of *H on Ag/Bi$_2$O$_2$CO$_3$ is 1.26 eV (Fig. 5c and d). Therefore, the HCOOH pathway is more energetically-favourable than the CO and H$_2$ pathways, leading to high HCOOH selectivity on Ag/Bi$_2$O$_2$CO$_3$.

Similarly, for Bi$_2$O$_2$CO$_3$, HCOOH is more easily generated than CO and H$_2$ (Fig. S14 and S15†). Notably, the energy barrier of *OCHO formation was reduced from 0.86 eV for Bi$_2$O$_2$CO$_3$ to 0.45 eV for Ag/Bi$_2$O$_2$CO$_3$, suggesting that the formation of HCOOH on Ag/Bi$_2$O$_2$CO$_3$ was easier than that on Bi$_2$O$_2$CO$_3$. To investigate the electronic structure of Ag/Bi$_2$O$_2$CO$_3$, charge density difference was also calculated. As shown in Fig. S16,† there is a strong interfacial interaction between Ag and Bi$_2$O$_2$CO$_3$, raising the valence state of Bi and enhancing the adsorption of *OCHO, consequently boosting the reaction activity of CO$_2$ to HCOOH.

Conclusions

In summary, we have successfully prepared Ag/Bi$_2$O$_2$CO$_3$ *via* an *in situ* transformation from Ag/Bi$_2$O$_3$. The prepared Ag/Bi$_2$O$_2$CO$_3$ exhibits excellent selectivity (FE$_{HCOOH}$ ≥90% over a

wide potential window) and satisfactory durability (no activity loss for 10 h) in the CO$_2$RR to HCOOH. XPS results and DFT calculations prove that a higher valence state of the Bi active site possesses optimal binding energy to form the key formate intermediate *OCHO, reducing the energy barrier of the RDS and enhancing the faradaic efficiency of HCOOH. These insights can be further exploited as design principles for other catalysts.

Author contributions

Wei Zheng: conceptualization, methodology, software, investigation, formal analysis, and writing – original draft; Changlai Wang: software, formal analysis, visualization, and writing – original draft; Jing Chen: methodology; Shi Chen: visualization; Zhiyu Lin: methodology; Minxue Huang: software and validation; Hao Huang: data curation and software; Yafei Qu: software, validation, and data curation; Peichen Wang: software, validation, and data curation; Lin Hu: writing – review & editing; Qianwang Chen: conceptualization, funding acquisition, resources, supervision, and writing – review & editing.

Conflicts of interest

There are no conflicts to declare.

Acknowledgements

References

1 M. Aresta, A. Dibenedetto and A. Angelini, *Chem. Rev.*, 2014, **114**, 1709–1742.

2 C. Xia, P. Zhu, Q. Jiang, Y. Pan, W. Liang, E. Stavitski, H. N. Alshareef and H. Wang, *Nat. Energy*, 2019, **4**, 776–785.

3 G. Lee, Y. C. Li, J.-Y. Kim, T. Peng, D.-H. Nam, A. S. Rasouli, F. Li, M. Luo, A. H. Ip, Y.-C. Joo and E. H. Sargent, *Nat. Energy*, 2021, **6**, 46–53.

4 Z. Zhang, M. Chi, G. M. Veith, P. Zhang, D. A. Lutterman, J. Rosenthal, S. H. Overbury, S. Dai and H. Zhu, *ACS Catal.*, 2016, **6**, 6255–6264.

5 G. Wen, D. U. Lee, B. Ren, F. M. Hassan, G. Jiang, Z. P. Cano, J. Gostick, E. Croiset, Z. Bai, L. Yang and Z. Chen, *Adv. Energy Mater.*, 2018, **8**, 1802427.

6 M. Huang, S. Gong, C. Wang, Y. Yang, P. Jiang, P. Wang, L. Hu and Q. Chen, *Angew. Chem., Int. Ed.*, 2021, **60**, 23002–23009.

7 F. Li, A. Thevenon, A. Rosas-Hernández, Z. Wang, Y. Li, C. M. Gabardo, A. Ozden, C. T. Dinh, J. Li, Y. Wang, J. P. Edwards, Y. Xu, C. McCallum, L. Tao, Z.-Q. Liang, M. Luo, X. Wang, H. Li, C. P. O'Brien, C.-S. Tan, D.-H. Nam, R. Quintero-Bermudez, T.-T. Zhuang, Y. C. Li, Z. Han, R. D. Britt, D. Sinton, T. Agapie, J. C. Peters and E. H. Sargent, *Nature*, 2020, **577**, 509–513.

8 X. Lv, L. Shang, S. Zhou, S. Li, Y. Wang, Z. Wang, T. Sham, C. Peng and G. Zheng, *Adv. Energy Mater.*, 2020, **10**, 2001987.

9 Y.-X. Duan, F.-L. Meng, K.-H. Liu, S.-S. Yi, S.-J. Li, J.-M. Yan and Q. Jiang, *Adv. Mater.*, 2018, **30**, 1706194.

10 S. Liu, X. F. Lu, J. Xiao, X. Wang and X. W. (David) Lou, *Angew. Chem., Int. Ed.*, 2019, **58**, 13828–13833.

11 W. Ma, J. Bu, Z. Liu, C. Yan, Y. Yao, N. Chang, H. Zhang, T. Wang and J. Zhang, *Adv. Funct. Mater.*, 2021, **31**, 2006704.

12 T. Tran-Phu, R. Daiyan, Z. Fusco, Z. Ma, R. Amal and A. Tricoli, *Adv. Funct. Mater.*, 2020, **30**, 1906478.

13 L. Yi, J. Chen, P. Shao, J. Huang, X. Peng, J. Li, G. Wang, C. Zhang and Z. Wen, *Angew. Chem., Int. Ed.*, 2020, **59**, 20112–20119.

14 D. Wu, X. Wang, X.-Z. Fu and J.-L. Luo, *Appl. Catal., B*, 2021, **284**, 119723.

15 P. Deng, H. Wang, R. Qi, J. Zhu, S. Chen, F. Yang, L. Zhou, K. Qi, H. Liu and B. Y. Xia, *ACS Catal.*, 2020, **10**, 743–750.

16 J. K. Nørskov, F. Abild-Pedersen, F. Studt and T. Bligaard, *Proc. Natl. Acad. Sci. U. S. A.*, 2011, **108**, 937–943.

17 G. Kresse and J. Hafner, *Phys. Rev. B: Condens. Matter Mater. Phys.*, 1993, **48**, 13115–13118.

18 G. Kresse and D. Joubert, *Phys. Rev. B: Condens. Matter Mater. Phys.*, 1999, **59**, 1758–1775.

19 J. P. Perdew, K. Burke and M. Ernzerhof, *Phys. Rev. Lett.*, 1996, **77**, 3865–3868.

20 A. M. Ferraria, A. P. Carapeto and A. M. B. do Rego, *Vacuum*, 2012, **86**, 1988–1991.

21 Y. Zhang, Y. Chen, R. Liu, X. Wang, H. Liu, Y. Zhu, Q. Qian, Y. Feng, M. Cheng and G. Zhang, *InfoMat*, 2023, **5**, e12375.

22 Y. Wang, B. Wang, W. Jiang, Z. Liu, J. Zhang, L. Gao and W. Yao, *Nano Res.*, 2022, **15**, 2919–2927.

23 M. Muñoz, P. Argoul and F. Farges, *Am. Mineral.*, 2003, **88**, 694–700.

24 M. Muoz, F. Farges and P. Argoul, *Physica Scripta*, 2005, 221.

25 K. Sun, J. Dong, H. Sun, X. Wang, J. Fang, Z. Zhuang, S. Tian and X. Sun, *Nat. Catal.*, 2023, **6**, 1164–1173.

26 Z. Chen, K. Mou, X. Wang and L. Liu, *Angew. Chem.*, 2018, **130**, 12972–12976.

27 J. Zhou, K. Yuan, L. Zhou, Y. Guo, M. Luo, X. Guo, Q. Meng and Y. Zhang, *Angew. Chem., Int. Ed.*, 2019, **58**, 14197–14201.

28 K. Fan, Y. Jia, Y. Ji, P. Kuang, B. Zhu, X. Liu and J. Yu, *ACS Catal.*, 2020, **10**, 358–364.